Calcium Dynamics, Buffering, and Buffer Saturation in the Boutons of Dentate Granule-Cell Axons in the Hilus

Meyer B. Jackson and Stephen J. Redman
Division of Neuroscience, John Curtin School of Medical Research, Canberra, ACT 0200, Australia

The axons of dentate gyrus granule cells form synapses in the hilus. Ca^{2+} signaling was investigated in the boutons of these axons using confocal fluorescence imaging. Boutons were loaded with various concentrations of the Ca^{2+} indicator Oregon Green BAPTA-1 by patch-clamping the cell bodies and allowing the dye to diffuse into the axon. Resting free [Ca^{2+}] started at 74 nM, rose to ~1 μM immediately after an action potential, and then decayed to rest with a time constant of 43 msec (all extrapolated to a dye concentration of zero). Action potential-induced [Ca^{2+}] rises were smaller in larger boutons, consistent with a size-independent Ca^{2+} channel density of 45/μm^2. Action potential-induced [Ca^{2+}] changes varied with dye concentration in a manner consistent with κ_E ~20 for the ratio of endogenous buffer-bound Ca^{2+} to free Ca^{2+}. During trains of action potentials, [Ca^{2+}] increments summed supralinearly by more than that expected from dye saturation. The amount of endogenous Ca^{2+} buffering declined as [Ca^{2+}] rose, and this saturation indicated a buffer with a dissociation constant of ~500 nM and a concentration of ~130 μM. This is similar to the dissociation constant of calbindin-D28K, a Ca^{2+}-binding protein that is abundant in dentate granule cells. Thus, calbindin-D28K is a good candidate for the Ca^{2+} buffer revealed by these experiments. The saturation of endogenous buffer can generate short-term facilitation by amplifying [Ca^{2+}] changes during repetitive activity. Buffer saturation may also be relevant to the presynaptic induction of long-term potentiation at synapses formed by dentate granule cells.

Key words: **nerve terminals; calcium dynamics; calcium buffers; hippocampus; dentate gyrus; calbindin-D28K; mossy fibers**

Introduction

Calcium ions enter a nerve terminal during presynaptic action potentials and bind to Ca^{2+} sensors to trigger neurotransmitter release. Cytoplasmic Ca^{2+} buffers compete for this Ca^{2+} to dampen the Ca^{2+} rise; Ca^{2+} sequestration and extrusion machinery restore Ca^{2+} to resting levels. By shaping the Ca^{2+} signal, the Ca^{2+}-regulating systems of a nerve terminal play an important role in controlling synaptic function. Cytoplasmic Ca^{2+} signaling can be investigated by imaging with fluorescent dyes. Most previous fluorometric studies of presynaptic Ca^{2+} fall into two distinct groups. Large nerve terminals are loaded by direct injection of Ca^{2+}-sensitive dye (Smith et al., 1988; Jackson et al., 1991; Helmchen et al., 1997), affording a degree of control over the cytoplasm and membrane. This method cannot be applied to the far more abundant nerve terminals of smaller size. Alternatively, small nerve terminals can be loaded by extracellular application of membrane-permeable dyes (Regehr and Tank, 1991a; Melamed et al., 1993; Umbach et al., 1998). This overcomes the size obstacle, but the dye concentration is difficult to control. A promising new approach to the study of Ca^{2+} in nerve terminals is to fill the cell body with dye and allow it to diffuse into the axon (DiGregorio and Vergara, 1997; Cox et al., 2000; Koester and Sakmann, 2000; Emptage et al., 2001). The dye concentration can thus be controlled even in small nerve terminals, provided that they are close enough to the cell body to fill during a recording. In addition, by filling a selected cell, the origin of the axon is unambiguous.

We have applied this new loading technique to the granule cells of the dentate gyrus. These cells give rise to the well known mossy fiber pathway of the hippocampus (Henze et al., 2000). Mossy fiber synapses exhibit both short- and long-term plasticity. Long-term potentiation (LTP) at these synapses outlasts short-term changes in presynaptic Ca^{2+} (Regehr and Tank, 1991b); however, short-term changes in synaptic strength correlate well with Ca^{2+} (Regehr et al., 1994). Mossy fiber boutons vary in size over a wide range, and the largest of these were recently patch-clamped (Geiger and Jonas, 2000). Although mossy fiber terminals in the hippocampal CA3 region are ~1 mm from the cell body and too far to be filled conveniently by this route, granule-cell axons branch extensively in the nearby hilus and display large numbers of boutons proximal to the cell body (Claiborne et al., 1986; Acsady et al., 1998). Granule cells form synapses in the hilus, indicating that these boutons constitute functional synaptic endings (Scharfman et al., 1990; Scharfman, 1993). Filling granule cells with Ca^{2+} indicators allowed us to follow the time course of [Ca^{2+}] after action potentials and characterize the endogenous Ca^{2+} buffers.

A quantitative description of how Ca^{2+} triggers neurotransmitter release depends on the knowledge of rapid spatially restricted transients in presynaptic Ca^{2+}. Current Ca^{2+}-imaging technology lacks the resolution to study these transients in small nerve terminals. Endogenous Ca^{2+} buffers are poorly understood, but they are likely to play an important role in shaping the spatiotemporal pattern of presynaptic Ca^{2+} (Yamada and Zucker, 1992; Roberts, 1994; Tank et al., 1995; Neher, 1998; Augustine, 2001; Burrone et al., 2002; Meinrenken et al., 2002). We

Received Nov. 13, 2002; revised Dec. 17, 2002; accepted Dec. 19, 2002.
We thank Garry Rodda for technical assistance.
Correspondence should be addressed to Meyer Jackson, Department Physiology, SMI 127, University of Wisconsin Medical School, 1300 University Avenue, Madison, WI 53706. E-mail: Mjackson@Physiology.wisc.edu.
 0270-6474/03/231612-10$15.00/0

analyzed the Ca^{2+} rises elicited by trains of action potentials and saw that the cytoplasmic buffering capacity declined as $[Ca^{2+}]$ rose. Thus, the Ca^{2+} buffers of granule-cell boutons saturate in a physiological range of intracellular $[Ca^{2+}]$.

Materials and Methods

Slice preparation. Animals that were 3–4 weeks of age were rendered unconscious with halothane and decapitated. The brain was removed; chilled in ice-cold cutting solution consisting of (in mM): 124 NaCl, 3.2 KCl, 1.25 NaH_2PO_4, 26 $NaCO_3$, 1 $CaCl_2$, 6 $MgCl_2$, 2 pyruvate, 3 ascorbate, and 10 glucose; and saturated with 95% O_2/5% CO_2. Slices 400 μm thick were cut with a vibratome, maintained for 30 min at 34°C immediately after cutting, and subsequently maintained at room temperature (~22°C) in artificial CSF (ACSF) for an additional 30 min before experiments. ACSF was identical to cutting solution but contained 2.5 mM $CaCl_2$, lacked ascorbate and pyruvate, and contained 1.3 mM $MgSO_4$ in place of $MgCl_2$.

Electrophysiology. Recordings were made at 28–30°C while perfusing slices with ACSF saturated with 95% O_2/5% CO_2. Granule cells were identified in the stratum granulosa using a Zeiss (Thornwood, NY) microscope with infrared-differential interference contrast optics. Cells visualized with the aid of Ca^{2+}-sensitive fluorescent dye (details below) showed the characteristic granule-cell morphology, with dendrites extending into the molecular layer and an axon extending into the hilus (see Fig. 1*A*). Granule cells were patch-clamped with an Axopatch 200C amplifier (Axon Instruments, Foster City, CA) using borosilicate glass patch pipettes filled with (in mM): 135 K-methylsulfate, 10 HEPES, 10 Na-phosphocreatine, 4 $MgCl_2$, 4 Na-ATP, 0.4 Na-GTP, pH 7.3, and 12.5–100 μM Oregon Green BAPTA-1 (OGB1) or 100 μM Oregon Green BAPTA-6F (OGB6F) (Molecular Probes, Eugene, OR). Pipette resistance ranged from 3 to 8 MΩ before recording. Recordings were made in current-clamp, and the resting potential was regularly checked. Action potentials were evoked either singly or in trains (1–2 sec, 20 Hz) using 1 msec current pulses.

Imaging and microscopy. Imaging was performed with a Zeiss LSM 510 laser-scanning confocal microscope. Light from an argon laser (488 nm) was used for illumination, and the FITC/GFP (green fluorescent protein) filter set prescribed for this microscope (dichroic, 488 nm; long-pass, 505 nm) selected fluorescent light and rejected laser lines. Before data acquisition, OGB1 was allowed to fill the axon for ≥15 and usually 30 min after break-in. When the time course of loading was followed, the dye fluorescence in proximal boutons reached a plateau within 15–30 min. Occasional checks of fluorescence intensity at ~5 min intervals confirmed the stability of dye concentration. The axon was visualized as in Figure 1*A* and systematically traced from the cell body. Boutons such as those in Figure 1*B–D* were located and lines for scanning were drawn through boutons that were perpendicular to the axon (see Fig. 1*D*). Excitation parameters were adjusted to minimize photo damage (laser intensity, <0.5% of 6 mW; scan duration, <1 msec; pixel size, 0.02–0.05 μm). For single action potentials, line scans were taken every 5 msec, with an action potential evoked 0.1 sec after the start of a 0.5 sec sampling episode. For trains, line scans were performed at 10 msec intervals, with a 20 Hz, 1–2 sec train initiated 0.1 sec after the start of a 1–2 sec sampling episode. With these settings, photo damage, as evidenced by an increase in resting brightness and a decline in evoked responses, was generally not apparent until >10–20 recordings were made from the same bouton. Only two recordings were needed to obtain useful information from a single bouton: a spike and a train. Trials were often repeated, but nearly all of the data presented here were obtained with less than five recordings per bouton.

Data analysis. Measurements of $[Ca^{2+}]$ follow the method of Maravall et al. (2000). Recordings were initially examined with the software that was provided with the microscope. The segment of each scanned line, which included the entire cross-sectional extent of a bouton (see Fig. 1*E1*, *E2*), was selected and averaged. Flanking segments well separated from the bouton on each side were used to estimate the background for each recording. Intracellular free $[Ca^{2+}]$ was calculated from background-subtracted fluorescence (f) as follows:

$$[Ca^{2+}] = K_d \frac{f - f_{min}}{f_{max} - f}. \quad (1)$$

The dissociation constant of OGB1 (K_d) was taken as 206 nM (Sabatini et al., 2002). The fluorescence under conditions in which all OGB1 is bound to Ca^{2+} (f_{max}) was determined from a plateau in fluorescence during trains of action potentials (see Results). The fluorescence for free OGB1 (f_{min}) was calculated from f_{max} assuming that $f_{max}/f_{min} = 6$ (Sabatini et al., 2002). Although this ratio depends on poorly defined aspects of the cellular environment, estimates of $[Ca^{2+}]$ are relatively insensitive to the exact value as long as f_{max}/f_{min} is a large value (Maravall et al., 2000).

For plotting and analysis of the decay kinetics of $[Ca^{2+}]$, fluorescence signals were transported to the computer program Origin (Microcal Software, Northampton, MA). $[Ca^{2+}]$ was computed from Equation 1, and the decay was fitted to a single exponential. Filtering was generally performed before fitting, although in several checks, filtering had no significant effect on the value of the time constant.

Endogenous Ca^{2+} buffers. Endogenous Ca^{2+} buffers were analyzed by a number of methods, starting with those of Neher and Augustine (1992), as adapted to a single-compartment model in which exchange of dye with the patch pipette or other regions of the cell is neglected (Helmchen et al., 1997; Sabatini et al., 2002). Buffers slow the decay of a $[Ca^{2+}]$ transient, and when the kinetic equations are linearized, the decay is exponential with a time constant:

$$\tau = \tau_0(1 + \kappa_E + \kappa_D). \quad (2)$$

τ_0 corresponds to γ/v from Neher and Augustine (1992) and reflects the activity of Ca^{2+} extrusion systems. This quantity can be thought of as the time constant for Ca^{2+} removal in the complete absence of buffering. κ_E and κ_D are the buffering capacities of the endogenous buffers (e.g., cytoplasmic Ca^{2+}-binding molecules) and the Ca^{2+}-sensitive dye (OGB1), respectively. These quantities represent the ratio of changes in concentrations of the Ca^{2+}-buffer complex to free Ca^{2+}. κ_D is computed from the dye concentration for a change from $[Ca^{2+}]_1$ to $[Ca^{2+}]_2$ as follows:

$$\kappa_D = \frac{\Delta[CaD]}{\Delta[Ca^{2+}]} = \frac{[D]_t K_d}{([Ca^{2+}]_1 + K_d)([Ca^{2+}]_2 + K_d)}. \quad (3)$$

The total dye concentration, $[D]_t$, was taken as [OGB1] in the patch pipette, and as noted above, care was taken to allow time for the dye to diffuse into the bouton under study. With κ_D from Equation 3 and τ determined from the decay of a $[Ca^{2+}]$ rise, κ_E can be determined by plotting τ versus κ_D and fitting to a line. According to Equation 2, the x-intercept is $-1 - \kappa_E$. κ_E can also be expressed in terms of $[B]_t$ and K_b, the concentration and dissociation constant of the endogenous buffer, by an analogy with Equation 3:

$$\kappa_E = \frac{\Delta[CaB]}{\Delta[Ca^{2+}]} = \frac{[B]_t K_b}{([Ca^{2+}]_1 + K_b)([Ca^{2+}]_2 + K_b)}. \quad (4)$$

An alternative method for determining κ_E uses a plot of the reciprocal of a $[Ca^{2+}]$ change versus κ_E, and is based on the following equation (Neher and Augustine, 1992):

$$\frac{1}{\Delta[Ca^{2+}]} = \frac{1 + \kappa_E + \kappa_D}{\Delta[Ca^{2+}]_t}. \quad (5)$$

In the present study, $\Delta[Ca^{2+}]_t$ will always be taken as the increment in total $[Ca^{2+}]$ (free plus bound) induced by an action potential. According to Equation 5, a linear fit to a plot of $1/\Delta[Ca^{2+}]$ versus κ_D once again gives the x-intercept as $-1 - \kappa_E$.

We developed a different method for analyzing $[Ca^{2+}]$ changes that is more easily extended to the treatment of saturable endogenous buffers. For an action potential producing an increment in total $[Ca^{2+}]$ of

$\Delta[Ca^{2+}]_t$, the initial and subsequent concentrations obey the following relationship:

$$[Ca^{2+}]_1\left(1 + \kappa_E + \frac{[D]_t}{K_d + [Ca^{2+}]_1}\right) + \Delta[Ca^{2+}]_t = [Ca^{2+}]_2\left(1 + \kappa_E + \frac{[D]_t}{K_d + [Ca^{2+}]_2}\right). \quad (6)$$

$[Ca^{2+}]_1$ and $[Ca^{2+}]_2$ are the two measured concentrations before and after an action potential. The terms in parentheses in Equation 6, when multiplied by $[Ca^{2+}]_1$ or $[Ca^{2+}]_2$, are easily recognized as free endogenous buffer-bound and dye-bound Ca^{2+}, respectively. Equation 6 thus expresses the conservation of Ca^{2+}.

Equation 6 can be extended to a model with a single endogenous Ca^{2+} buffer, B:

$$[Ca^{2+}]_1\left(1 + \frac{[B]_t}{K_b + [Ca^{2+}]_1} + \frac{[D]_t}{K_d + [Ca^{2+}]_1}\right) + \Delta[Ca^{2+}]_t = [Ca^{2+}]_2\left(1 + \frac{[B]_t}{K_b + [Ca^{2+}]_2} + \frac{[D]_t}{K_d + [Ca^{2+}]_2}\right). \quad (7)$$

K_b and $[B]_t$ are as in Equation 4. Equation 7 differs from Equation 6 in the replacement of κ_E by a term to reflect the saturation of the endogenous buffer.

The models represented by Equations 6 and 7 were fitted to data by comparing a measured value of $[Ca^{2+}]_2$ with a value of $[Ca^{2+}]_2$ calculated from a measured value of $[Ca^{2+}]_1$ and the free parameters. The calculated value of $[Ca^{2+}]_2$ was obtained by solving the corresponding quadratic (Eq. 6) or cubic (Eq. 7) equation. The sum-of-squares error between calculated and measured $[Ca^{2+}]_2$ was then minimized by varying the free parameters. For Equation 6, two free parameters, κ_E and $\Delta[Ca^{2+}]_t$, were varied. For Equation 7, three parameters, K_b, $[B]_t$, and $\Delta[Ca^{2+}]_t$ were varied. Both the solution of the equations (numerically) and the fitting were performed with the computer program Mathcad (Mathsoft, Cambridge, MA). Fitting with Mathcad does not provide the errors in parameters, but errors of the fit were computed as the square root of the sum-of-squares error of $[Ca^{2+}]_2$. Curve fits to simpler models performed within Origin yielded very similar values of parameters and also provided errors. The equations above were extended to the analysis of $[Ca^{2+}]$ rises during trains, but this analysis is best described together with the data in Results.

Results

When granule cells were patch-clamped with pipettes containing OGB1, a loaded axon became visible within a few minutes. In ~50% of the recordings, the axon terminated at the surface of the slice <100 μm from the cell body, indicating that the axon was cut during slice preparation. In ~25% of the recordings, a ~100 μm segment of axon was visible. A few swellings were often found quite close to the cell body, and recordings from these swellings were included in this study. In the remaining ~25% of granule cells, a long axon was visible with many irregularly distributed swellings and occasional branches (Fig. 1*A*). These fluorescence images resembled dentate granule-cell axons visualized by other histological techniques (Claiborne et al., 1986; Acsady et al., 1998), and the majority of the data presented here were from axons such as these. Closer examination of axonal segments under higher magnification revealed structures with the appearance of *en passant* presynaptic boutons (Fig. 1*B–D*), with diameters ranging from 0.5 to 3.5 μm.

An action potential evoked by a current pulse produced fluorescence increases in dendritic shafts, spines, axons, and boutons. Attention here focused on boutons; no effort was made to compare boutons with other regions. Figure 1*D* illustrates a bouton selected for study with the line of scanning indicated. The fluo-

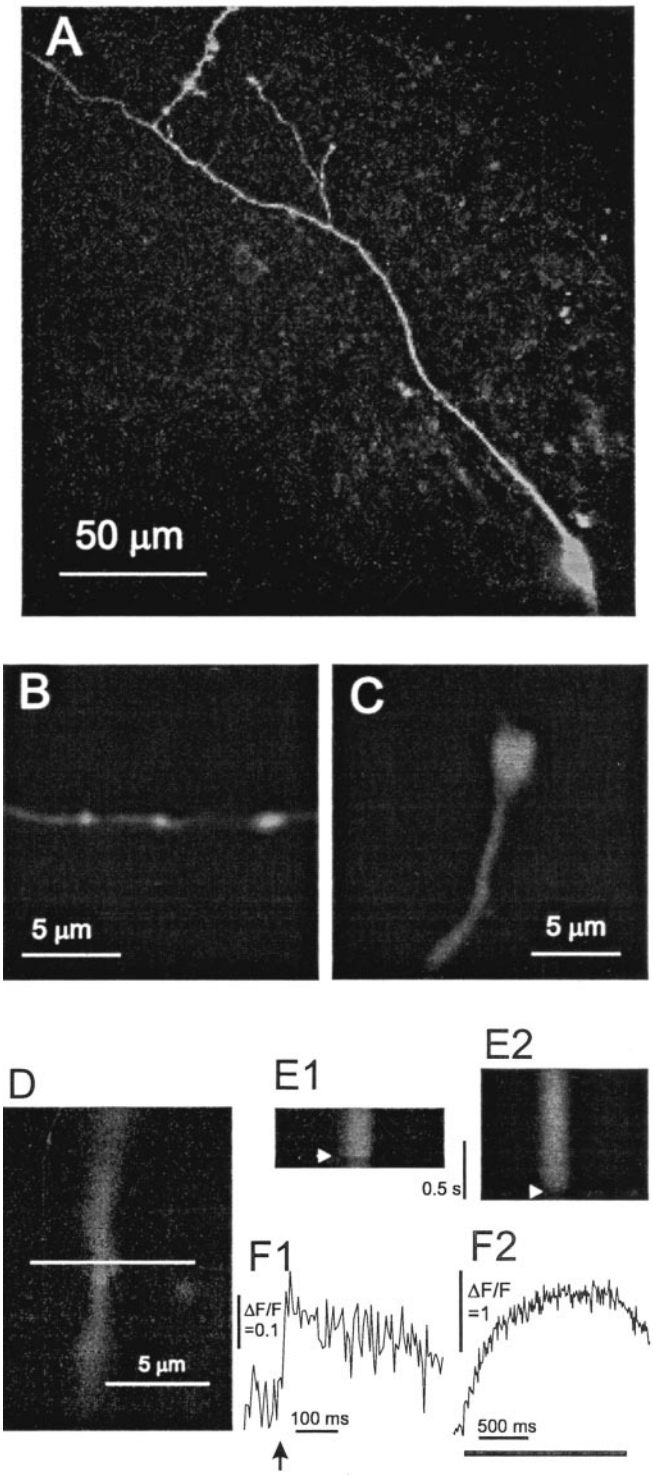

Figure 1. Confocal fluorescence micrographs of dentate granule cells filled with OGB1. *A*, A cell body and long-branched stretch of axon visualized from a z-stack projection spanning a depth of 40 μm. *B*, *C*, Segments of axon with three boutons (*B*) and one bouton (*C*) are shown. *D*, A bouton selected for recordings is shown with the line selected for scanning. *E*, Line scans show fluorescence increases evoked by an action potential (*E1*) and a train of action potentials at 20 Hz (*E2*). The *horizontal axis* is the position along the line in *D*. The *vertical axis* is time. The *arrowhead* indicates the time of the action potential in *E1* and the start of the train in *E2*. *F*, Fluorescence in the segment spanning the bouton was averaged and plotted versus time for the action potential experiment in *E1* and the train experiment in *E2*. The *arrow* in *F1* shows the time of the action potential, and the *bar* in *F2* shows the time for the train. Fluorescence traces were background subtracted and normalized to give $\Delta F/F$. [OGB1]: *A*, *B*, 100 μM; *C–F*, 50 μM.

rescence change resulting from an action potential evoked in the cell body can be seen in the vertical succession of lines (Fig. 1*E1*). A small fluorescence increase across the bouton follows the action potential nearly synchronously (indicated by the *arrow*). Averaging the fluorescence in the segment of the line spanning the bouton shows this fluorescence change more clearly (Fig. 1*F1*). When a current step applied to the cell body was subthreshold for action potential generation, no fluorescence change was detected in axonal swellings, indicating that passive spread of brief depolarizations cannot elicit detectable Ca^{2+} influx at these remote sites.

The following observations were not studied in depth but are noted here because they confirm previous studies of axons in other types of neurons. First, although most of the data collection was at 5 msec sampling intervals, a few recordings at 1–2 msec intervals indicated that the Ca^{2+} rise was complete within 1–2 msec. This is as rapid as that observed previously in boutons of cortical pyramidal cells (Cox et al., 2000; Koester and Sakmann, 2000). Second, in recordings at distal sites beyond initial boutons and branch points, fluorescence signals followed somatic action potentials with high fidelity. In no instance was a failure evident, either in a single action potential or the first few action potentials of 20 Hz trains. Thus, action potentials reliably invade the extensive arbors of granule-cell axons, as they do in pyramidal cell axons (Cox et al., 2000; Koester and Sakmann, 2000; Emptage et al., 2001)

Determination of f_{max}

Conversion of fluorescence to $[Ca^{2+}]$ with Equation 1 requires an estimate of f_{max}, the fluorescence when all of the OGB1 is Ca^{2+} bound. To saturate the dye, we used 20 Hz trains of action potentials. Figure 1*E2* shows a series of lines at 10 msec intervals with a train initiated after 100 msec. The fluorescence increase (Fig. 1*F2*) exceeded that elicited by a single action potential (Fig. 1*F1*), by a factor of >20 in this case. The increments induced by individual action potentials were resolved early in the train. In this experiment, performed with 50 μM OGB1, fluorescence reached a plateau in slightly <1 sec after the start of the train and started to decay only when the train had terminated. When a lower concentration (25 μM) of OGB1 was used, the plateau was reached in ~0.5 sec (Fig. 2*A*). When a higher concentration (100 μM) was used, the time to reach a plateau was longer (Fig. 2*B*). These results indicate that the plateau in fluorescence with lower OGB1 concentrations is reached while $[Ca^{2+}]$ continues to rise. This supports the interpretation of the plateau as a saturation of the dye.

A similar argument can be made using a lower affinity dye. When a train was applied to a bouton filled with 100 μM OGB6F (K_d, ~3 μM), fluorescence continued to rise for >1 sec (Fig. 2*C*). This means that the saturation of fluorescence seen with OGB1 occurs as $[Ca^{2+}]$ continues to rise. Thus, the plateau in fluorescence reflects saturation of the dye rather than stabilization of $[Ca^{2+}]$ that might result from abatement of Ca^{2+} entry or compensation of Ca^{2+} entry by removal or sequestration. This supports the use of trains of action potentials to estimate f_{max}. This is confirmed by the results below on resting free $[Ca^{2+}]$, and by the observation that once the plateau is reached, deflections in fluorescence synchronous with action potentials cannot be detected, even in averages of many trains (see Fig. 5*A*).

Resting free $[Ca^{2+}]$

With f_{max} determined from a train, and $f_{min} = f_{max}/6$ (see Materials and Methods), we can use Equation 1 and the initial fluorescence to estimate $[Ca^{2+}]_0$, the resting free $[Ca^{2+}]$ within a bouton. $[Ca^{2+}]_0$ is plotted for four different values of [OGB1] in Figure 2*D*. All of the values are statistically indistinguishable, and a linear regression analysis showed no statistically significant correlation. This indicates that the dye does not alter $[Ca^{2+}]_0$. We can further say that the trains saturate OGB1 to a similar degree regardless of its concentration, supporting the measurement of f_{max} from these trains. From these data, our best estimate of $[Ca^{2+}]_0$ is the [OGB1] = 0 intercept from a linear least-squares fit. This value was 74 ± 9 nM.

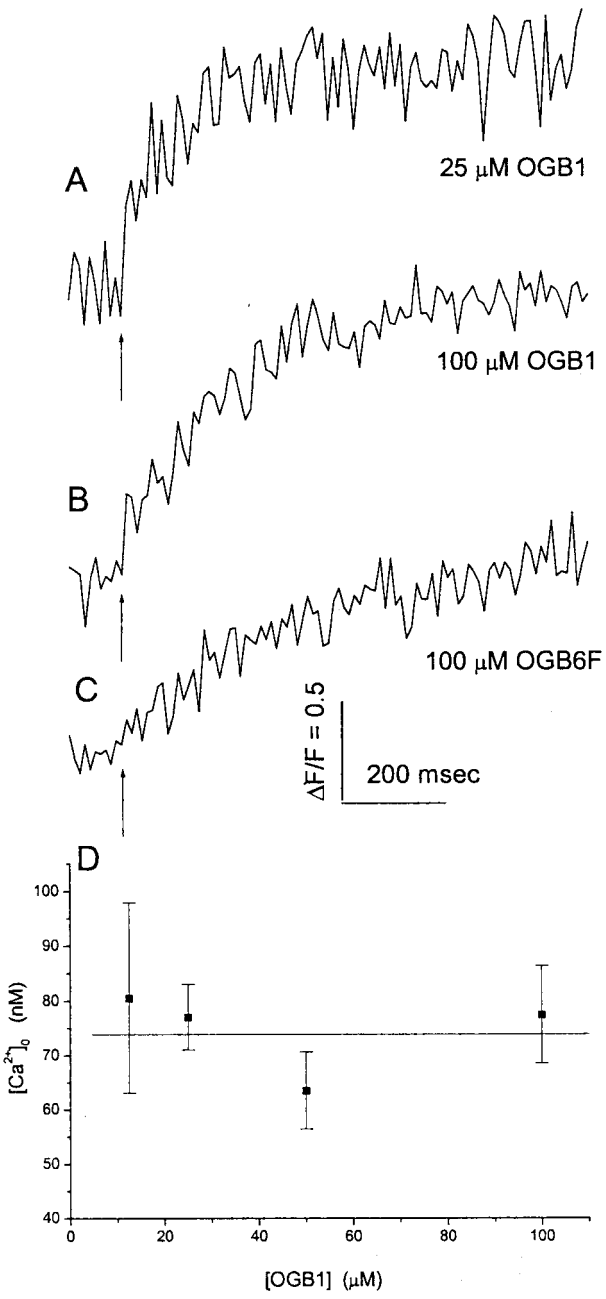

Figure 2. Fluorescence responses to trains of action potentials at 20 Hz illustrate the different rates of fluorescence rise for different intracellular dye solutions (indicated below each *trace*). Trains were initiated at the *arrow*. *A–C*, Recording of pipettes containing 25 μM OGB1 (*A*), 100 μM OGB1 (*B*), and 100 μM OGB6F (*C*). Fluorescence was averaged within a region of a bouton scanned by a *line* as in Figure 1*F2*. *D*, Resting $[Ca^{2+}]_0$, computed from the initial and maximal fluorescence using Equation 1, is plotted versus patch pipette [OGB1]. SE is shown with 6–54 measurements.

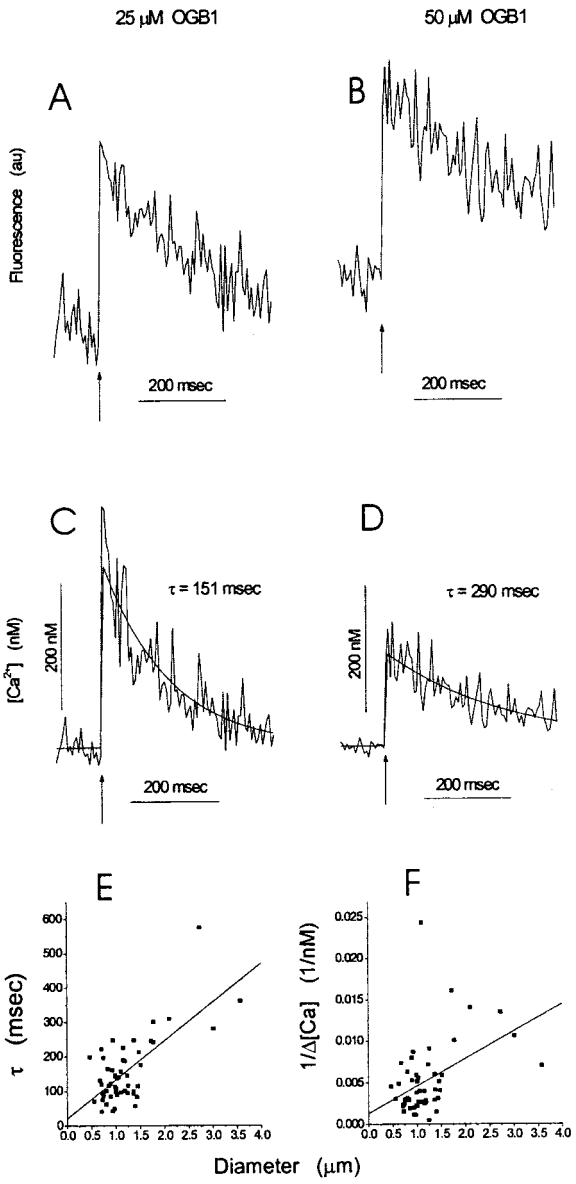

Figure 3. Fluorescence and $[Ca^{2+}]$ for two different values of [OBG1]. Action potentials were initiated at the *arrow*. *A–D*, Fluorescence traces in *A* and *B* were converted to $[Ca^{2+}]$ in *C* and *D*, respectively, using Equation 1. Exponential fits to $[Ca^{2+}]$ are shown together with estimates of τ. *E*, *F*, Plots of the time constant for $[Ca^{2+}]$ after an action potential (*E*) and the reciprocal of the peak change in $[Ca^{2+}]$ (*F*) versus bouton diameter; both plots were fitted to *lines*. The correlations were statistically significant with $p < 0.001$ for both plots. The slope of the *line* in *F* was used to calculate the Ca^{2+}-channel density (see Results).

The value of $[Ca^{2+}]_0$ was independent of bouton size. Bouton diameter was estimated from a plot of the fluorescence versus the position in line scans. A plot with 54 measurements made with 25 μM OGB1 showed no significant correlation between $[Ca^{2+}]_0$ and bouton diameter ($p = 0.21$; data not shown).

Action potential evoked $[Ca^{2+}]$ changes

Both action potential-induced fluorescence changes (Fig. 1*F1*) and train-induced fluorescence changes (Fig. 1*F2*) were recorded from individual boutons. f_{max} was determined for each bouton and used to convert fluorescence to free $[Ca^{2+}]$ by Equation 1. Fluorescence and $[Ca^{2+}]$ versus time is shown in Figure 3, *A* and *C*, for a bouton filled with 25 μM OGB1, and in Figure 3, *B* and *D*, for a bouton filled with 50 μM OGB1. The decays in $[Ca^{2+}]$ were well fitted by a single exponential function for both concentrations of OGB1 (Fig. 3*C*,*D*). These results illustrate two important effects of dye on the shape of the Ca^{2+} signal. Increasing the dye concentration reduces the amplitude of the Ca^{2+} rise and slows the recovery. These features are well known consequences of increased Ca^{2+} buffering (Neher, 1995) and will be exploited in an analysis of endogenous Ca^{2+} buffers below.

We made a larger number of measurements using 25 μM OGB1, because this concentration presented the best tradeoff between obtaining strong fluorescence signals and reducing dye-induced perturbations of $[Ca^{2+}]$. With 54 such measurements, we could see that the time constant for decay (Fig. 3*E*) as well as the reciprocal of the action potential-induced change in free $[Ca^{2+}]$ (Fig. 3*F*) varied with bouton size. Both plots showed highly significant correlations, with $p < 0.001$ from a linear least-squares fit. Thus, $[Ca^{2+}]$ rises are smaller and decays are slower in larger boutons. A similar correlation was obtained in dendritic spines for the amplitude of the change in free $[Ca^{2+}]$ and interpreted in terms of a fixed density of Ca^{2+} channels (Holthoff et al., 2002). Likewise, the correlation between the decay time constant and bouton size in Figure 3*E* could reflect a constant pump density.

A membrane Ca^{2+}-channel density that is independent of bouton size predicts a linear relationship between the quantities plotted in Figure 3*F*; the slope can be used to estimate this density. The change in number of moles of Ca^{2+} (total) within a bouton, Δm_{Ca}, is equal to the number of moles of Ca^{2+} that enters a bouton per Ca^{2+} channel, φ, times the number of Ca^{2+} channels, N, as follows:

$$\Delta m_{Ca} = \phi N. \quad (8)$$

If the density of Ca^{2+} channels is denoted as ρ_{Ca} and a spherical geometry is assumed, we can obtain the following:

$$\frac{1}{\Delta[Ca^{2+}]_t} = \frac{d}{6\phi\,\rho_{Ca}}, \quad (9)$$

where d is diameter, and as defined in Materials and Methods, $\Delta[Ca^{2+}]_t$ is the sum of the concentration increases in free and bound Ca^{2+}. Substituting $\Delta[Ca^{2+}]_t = \Delta[Ca^{2+}]_{free}(1 + \kappa_E + \kappa_D)$ (from Eq. 5) into Equation 9 then gives a linear relationship for interpreting Figure 3*F* with a slope of $(1 + \kappa_E + \kappa_D)/6\varphi\rho_{ch}$. For φ we took the value used by Koester and Sakmann (2000) based on the estimate that each Ca^{2+} channel passes 0.2 pA for 0.2 msec during an action potential. This gave 125 Ca^{2+} ions or 2.1×10^{-22} mol of Ca^{2+}. The slope in Figure 3*F* was 0.0033 $nM^{-1}\ \mu m^{-1}$. Equation 3 gave $\kappa_D = 43$ for these experiments. Based on the analysis of endogenous Ca^{2+} buffers presented below, we can take $\kappa_E = 20$ based on an analysis in terms of nonsaturable buffer, or $\kappa_E = 124$ computed with Equation 4 from our best estimates of the K_b and $[B]_t$ of the endogenous buffer. This gives a Ca^{2+} channel density of $\rho_{Ca} = 17/\mu m^2$ or $\rho_{Ca} = 45/\mu m^2$, respectively. Because data presented below indicate that the endogenous buffer is saturable, the second value is more reliable. The significance of different κ_E values for saturable and nonsaturable buffers will be discussed below.

$[Ca^{2+}]$ rises and endogenous Ca^{2+} buffers

To estimate the strength of endogenous Ca^{2+} buffers in bouton cytoplasm, we first examined a plot of the time constant for $[Ca^{2+}]$ decay from fits (Fig. 3*C*,*D*) versus κ_D (Eq. 3) (Fig. 4*A*). A linear fit based on Equation 2 yielded $\kappa_E = 18$ from the $\tau = 0$ intercept. The reciprocal of the action potential-induced $[Ca^{2+}]$

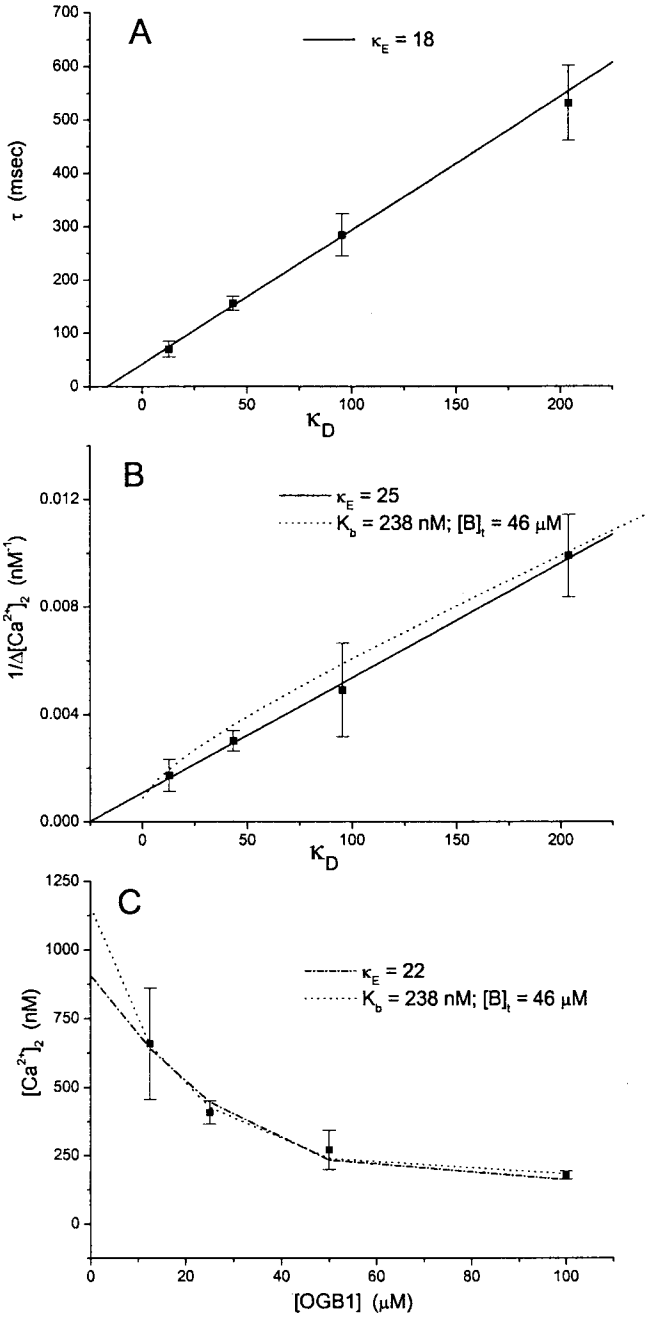

Figure 4. *A*, The time constant for $[Ca^{2+}]$ decay (from fits such as those in Fig. 3) was averaged for different values of [OGB1] and plotted versus average κ_D (from Eq. 3). The best fitting *line* (Eq. 2) gave $\kappa_E = 18$. *B*, Plot of the reciprocal of the action potential-induced Ca^{2+} change ($1/\Delta[Ca^{2+}]$) versus κ_D. The best fitting *line* (Eq. 5) gave $\kappa_E = 25$. *Dotted curve*, The prediction based on Equation 7, with K_b and $[B]_t$ obtained from the fit of Equation 7 to the data in *C*. *C*, Plot of peak free $[Ca^{2+}]$ after an action potential versus [OGB1]. The *dashed curve* represents $[Ca^{2+}]_2$ from Equation 6, with $\kappa_E = 22$ and $\Delta[Ca^{2+}]_t = 19$ μM from the best fits. The *dotted curve* represents the fit to Equation 7, which gave $K_b = 238$, $[B]_t = 46$ μM, and $\Delta[Ca^{2+}]_t = 29$ μM.

rise was plotted versus κ_D, and a linear fit based on Equation 5 yielded a similar value for a κ_E of 25 (Fig. 4*B*). The prediction of a model involving buffer saturation to be discussed below is also shown (Figure 4*B*, *dotted curve*).

We introduced a new method of analyzing Ca^{2+} buffers based on Equation 6 from Materials and Methods, with resting free $[Ca^{2+}]$ as $[Ca^{2+}]_1$ and the peak free $[Ca^{2+}]$ after an action potential as $[Ca^{2+}]_2$. Given $[Ca^{2+}]_1$, Equation 6 was solved for $[Ca^{2+}]_2$, and this value was compared with the measured value of $[Ca^{2+}]_2$. The parameters κ_E and $\Delta[Ca^{2+}]_t$ were then varied to minimize the error between calculated and measured $[Ca^{2+}]_2$. Measured $[Ca^{2+}]_2$ is plotted versus the dye concentration in Figure 4*C*. The calculated values of $[Ca^{2+}]_2$ obtained from the fit are represented by the *dashed curve*. The model fits the data very well, yielding $\kappa_E = 22$ and $\Delta[Ca^{2+}]_t = 19$ μM. Thus, the κ_E values determined by the three methods represented in Figure 4 are in reasonable agreement with one another. This comparison indicates that the decay time constants are reasonably well approximated by Equation 2 and are therefore not distorted by factors such as diffusion of Ca^{2+} to neighboring regions.

We next analyzed the data in Figure 4*C* using a model that includes a single endogenous buffer species with a saturable binding site (Eq. 7). This model was fitted to the data, yielding $[B]_t = 46$ μM, $K_b = 238$ nM, and $\Delta[Ca^{2+}]_t = 29$ μM. The computed values of $[Ca^{2+}]_2$ (Fig. 4*C*, *dotted curve*) are again in good agreement with this experiment. The error for the fit was reduced 40% compared with that achieved in Equation 6, but this model has one more free parameter. Both models give fits that fall close to the data points, so we conclude that the data presented in Figure 4*C* are consistent with either nonsaturating or saturating endogenous buffers.

Both saturating and nonsaturating models also fitted the plot of $1/\Delta[Ca^{2+}]$ versus κ_D in Figure 4*B*, in which the prediction of a saturable buffer based on Equation 7 is drawn as a *dotted curve*. This plot indicates that a saturable endogenous Ca^{2+} buffer predicts nearly linear behavior over a wide range of κ_D values. It is thus once again difficult to distinguish models with saturating and nonsaturating buffers. Furthermore, the values of κ_E calculated from Equation 5 with endogenous buffer properties that generated the *dotted curve* in Figure 4*B* range from 136 to 37 for $[Ca^{2+}]$ rises ranging from 0.1 to 1 μM. A saturable buffer with a much higher effective κ_E value can replicate the behavior of a nonsaturable buffer with a lower κ_E value. Thus, κ_E values derived from an analysis based on Equation 5 will be incorrect if a cell contains a buffer that saturates in the range of $[Ca^{2+}]$ under study (see Discussion).

The *y*-intercept in Figure 4*A* gives a dye-independent value for the time constant of Ca^{2+} removal $\tau_0(1 + \kappa_E) = 43 \pm 6$ msec (from Eq. 2). τ_0 is then computed as 2.4 msec, using the κ_E value obtained from the same plot. The magnitude of the rise in free $[Ca^{2+}]$, induced by an action potential for zero added dye, was computed with Equations 6 and 7 (using the parameters obtained from the fits) as 0.91 and 1.16 μM, respectively.

Summation of $[Ca^{2+}]$ rises and endogenous buffer saturation

During trains of action potentials we could resolve a series of steps in fluorescence associated with sequential action potential-induced $[Ca^{2+}]$ rises (Figs. 1*F2*, 2*A–C*). The later steps in the train start from higher levels of $[Ca^{2+}]$, in which there should be fewer Ca^{2+}-binding sites available within a bouton, because a greater fraction of those Ca^{2+}-binding sites should be occupied. These data thus contain information about Ca^{2+} buffer saturation. To analyze these trains quantitatively, the fluorescence signals from many nerve terminals were normalized to their maxima and averaged together. Figure 5*A* shows this average for all 15 bouton recordings made with 50 μM OGB1 (from four cells). This figure shows that the second action potential in the train elevated $[Ca^{2+}]$ from 124 to 290 nM. We could thus estimate the action potential-induced change in free $[Ca^{2+}]$ for a series of steps until f/f_{max} exceeded ~0.85 and free $[Ca^{2+}]$ exceeded ~1

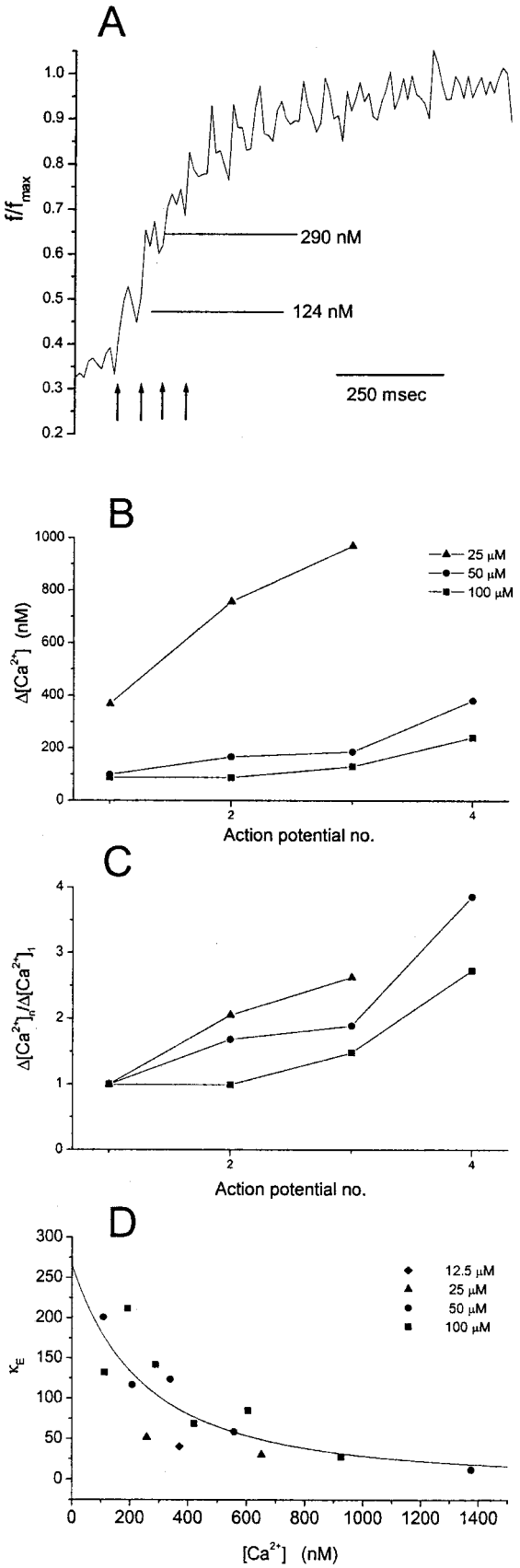

Figure 5. *A*, Fluorescence versus time during a train (*arrows* indicate the first four action potentials, continuing at 50 msec intervals). In 15 experiments with 50 μM OGB1, the fluorescence was normalized to the maximum and averaged. Computed free $[Ca^{2+}]$ immediately before and after the second action potential is shown to illustrate an example of $[Ca^{2+}]_1$ and $[Ca^{2+}]_2$ used to calculate κ_E in Equation 10. *B*, Increments in free $[Ca^{2+}]$ such as these are plotted versus action potential number in the train. Means similar to those in *A* were determined for seven boutons from three cells with 12.5 μM OGB1, 54 boutons from eight cells with 25 μM OGB1, and 11 boutons from eight cells with 100 μM OGB1. *C*, $[Ca^{2+}]$ increments normalized to the first increment of the train illustrate the supralinear summation of $[Ca^{2+}]$. *D*, Plot of κ_E versus $[Ca^{2+}]$. κ_E was calculated from Equation 10 ($\Delta[Ca^{2+}]_t = 30$ μM) for action potential-induced increases in $[Ca^{2+}]$. $[Ca^{2+}]$ was $0.5([Ca^{2+}]_1 + [Ca^{2+}]_2)$. The *curve* is the fit of Equation 11, with $K_b = 490$ nM and $[B]_t = 130$ μM. Linear regression yielded $p < 0.005$ for this plot. The *points* were derived from the first six action potentials in the train response with 100 μM OGB1, the first five action potentials in the train response with 50 μM OGB1, the first two action potentials in the train response with 25 μM OGB1, and the first action potential with 12.5 μM OGB1.

μM. Higher concentrations were subject to large errors because of the small value of the denominator in Equation 1.

The increases in free $[Ca^{2+}]$ are plotted in Figure 5*B* for 25, 50, and 100 μM OGB1. It can be seen that later action potentials always induce greater increases in free $[Ca^{2+}]$. This is illustrated more clearly in Figure 5*C*, with the $[Ca^{2+}]$ increments normalized to the first for each concentration of OGB1. Thus, the $[Ca^{2+}]$ rises produced by successive action potentials were supralinear, and this trend was evident for all three values of [OGB1]. (With 12.5 μM OGB1, the fluorescence rise during a train was so rapid that $[Ca^{2+}]$ after the second action potential could not be accurately measured; f/f_{max} was 0.92.)

One possible explanation for these supralinear increases in $[Ca^{2+}]$ is the saturation of OGB1. With a K_d of 206 nM, we would expect to see a reduction of buffering by this dye as $[Ca^{2+}]$ rises through its observed range. However, two other possibilities for the supralinear increases in $[Ca^{2+}]$ are changes in $\Delta[Ca^{2+}]_t$ and saturation of endogenous Ca^{2+} buffers. Because the effect of dye saturation can be calculated precisely, we can test the hypothesis of endogenous buffer saturation, subject to the assumption of constant $\Delta[Ca^{2+}]_t$. The issue of variation in $\Delta[Ca^{2+}]_t$ will be considered in the Discussion.

Taking Equation 6, we can solve for κ_E:

$$\kappa_E = \frac{[Ca^{2+}]_1\left(1 + \frac{[D]_t}{K_d + [Ca^{2+}]_1}\right) + \Delta[Ca^{2+}]_t - [Ca^{2+}]_2\left(1 + \frac{[D]_t}{K_d + [Ca^{2+}]_2}\right)}{[Ca^{2+}]_2 - [Ca^{2+}]_1}. \quad (10)$$

This equation can be used to calculate κ_E for each pair of $[Ca^{2+}]_1$ and $[Ca^{2+}]_2$ in the progression of steps during a train (Fig. 5*A*), provided that we have an estimate of $\Delta[Ca^{2+}]_t$. The analysis from Figure 4*C* yielded values for $\Delta[Ca^{2+}]_t$ of 19 and 29 μM, but the value of 19 μM was based on a model that assumes no saturation of the endogenous buffer (Eq. 6) and is therefore less reliable (see Discussion). Thus, we favor the value of 29 μM. This choice was confirmed by analysis of additional data from measurements with much higher dye concentration, in which the influence of endogenous buffers should be very small. We performed a limited set of measurements with 250 μM OGB1, from which we estimated $[Ca^{2+}]_0 = 91 \pm 15$ nM and a peak action potential-induced free $[Ca^{2+}]$ change of 72 ± 15 nM ($n = 5$). From these values, Equation 6 and 7, without the endogenous buffer term, gave $\Delta[Ca^{2+}]_t = 34$ μM. We therefore selected $\Delta[Ca^{2+}]_t = 30$ μM for most of our analyses but conducted checks with other values as well.

κ_E computed from Equation 10 is plotted versus $[Ca^{2+}]$, taken as $0.5([Ca^{2+}]_1 + [Ca^{2+}]_2)$ in Figure 5*D*. If the endogenous buffers failed to saturate in the range of $[Ca^{2+}]$ spanned in these experiments, the plot would be a horizontal line with no correlation between κ_E and $[Ca^{2+}]$. Figure 5*D* reveals a strong inverse correlation between κ_E and $[Ca^{2+}]$, with $p < 0.005$. The decrease in κE with increasing $[Ca^{2+}]$ suggests that the endogenous buffers are saturated by rising $[Ca^{2+}]$.

To estimate the concentration and dissociation constant of the saturable Ca^{2+} buffer implicated in Figure 5*D*, these data were analyzed in two ways. First, the *points* plotted in Figure 5*D* were fitted to the equation:

$$\kappa_E = \frac{[B]_{total} K_b}{([Ca^{2+}] + K_b)^2}, \quad (11)$$

κ_E is derived from Equation 4 using a single $[Ca^{2+}] = 0.5([Ca^{2+}]_1 + [Ca^{2+}]_2)$. The best fit is drawn in Figure 5*D*, with $[B]_t = 130 \pm 28$ μM and $K_b = 490 \pm 220$ nM. The geometric mean of $[Ca^{2+}]_1$ and $[Ca^{2+}]_2$ was also used for $[Ca^{2+}]$ rather than the arithmetic mean because of the product in the denominator of Equation 11. The fit produced the same results. When the analysis was performed with different values of $\Delta[Ca^{2+}]_t$, the inverse correlation was still strong ($p < 0.01$ for all the plots), and values for $[B]_t$ and K_b changed by less than a factor of 2. $[B]_t = 75 \pm 33$ μM and $K_b = 850 \pm 640$ nM for $\Delta[Ca^{2+}]_t = 20$ μM; $[B]_t = 191 \pm 32$ μM and $K_b = 414 \pm 160$ nM for $\Delta[Ca^{2+}]_t = 40$ μM.

To avoid using the mean $[Ca^{2+}]$ in Figure 5*D* and Equation 11, an analysis was conducted on the triplets of $[Ca^{2+}]_1$, $[Ca^{2+}]_2$, and κ_E (from Eq. 10). The constraint for fitting was set up with Equation 4. For the 14 *points* plotted in Figure 5*D*, the parameters $[B]_t$ and K_b were varied to minimize the error between κ_E from Equation 4 (a theoretical value) and κ_E from Equation 10 (an experimental value). This fit yielded very similar results ($K_b = 527$ nM and $[B]_t = 130$ μM with an $\Delta[Ca^{2+}]_t = 30$ μM). Similar results were obtained with $\Delta[Ca^{2+}]_t = 20$ μM ($K_b = 906$ nM and $[B]_t = 76$ μM) and $\Delta[Ca^{2+}]_t = 40$ μM ($K_b = 450$ nM and $[B_t] = 190$ μM). Because there is uncertainty about whether the affinity of the dye is altered by the cellular environment, we recalculated κ_E from Equation 10 using $K_d = 170$ and 240 nM for OGB1 instead of using 206 nM [the K_d of another Ca^{2+} indicator, fura-2, varies within this range in different *in vivo* environments (Neher, 1995)]. The inverse correlation between κ_E and $[Ca^{2+}]$ was maintained ($p < 0.005$) and the values for K_b and $[B]_t$ were not affected significantly.

In summary, $[Ca^{2+}]$ rises during trains indicate that an endogenous cytoplasmic Ca^{2+} buffer saturates as $[Ca^{2+}]$ increases from rest to 1 μM. The saturation was clear and significant for a range of values of $\Delta[Ca^{2+}]_t$ and for several variations in the analysis. With 30 μM as our best estimate of $\Delta[Ca^{2+}]_t$, K_b is ~500 nM and $[B]_t$ is ~130 μM.

Discussion

This study investigated Ca^{2+} signaling in boutons on axons arising from dentate gyrus granule cells. Axons were filled with fluorescent dye through the cell body by a patch electrode. This made it possible to measure a number of important quantities associated with Ca^{2+} signaling in single boutons while controlling dye concentration. This work extends previous methodology (DiGregorio and Vergara, 1997; Cox et al., 2000; Koester and Sakmann, 2000; Emptage et al., 2001) and demonstrates that loading of axons through the cell body can serve as a powerful general approach for studying Ca^{2+} signaling in nerve terminals. In principle, any neuron that forms synapses within a few hundred micrometers of the cell body should be amenable to this method.

Resting free Ca^{2+} ($[Ca^{2+}]_0$) was 74 nM and independent of dye concentration (Fig. 2*D*). The added buffering of the dye altered the speed and magnitude of responses but left $[Ca^{2+}]_0$ unchanged. This supports the idea that resting Ca^{2+} reflects the set point of a regulatory system that operates through a homeostatic response to free Ca^{2+}. The bouton size independence of $[Ca^{2+}]_0$ suggests that the Ca^{2+} regulation machinery (pumps and channels) is distributed uniformly.

Extrapolations to zero dye indicated that $[Ca^{2+}]$ rises to ~1 μM after an action potential (Fig. 4*C*) and then decays with a time constant of 43 msec. In guinea pig mossy fibers loaded with fura-2 AM, the action potential-induced $[Ca^{2+}]$ rise was 10–50 nM and the decay time constant was ~1 sec (Regehr et al., 1994). Although factors such as species, animal age, temperature, and methodology could contribute to the differences between these values and ours, we note that if the buffering strength of the fura-2 in the previous experiments exceeded the endogenous buffering strength by 25-fold, our estimates of both the $[Ca^{2+}]$ change and the time constant for decay would be in qualitative agreement.

Ca^{2+}-channel density

The reciprocal of the action potential-induced $[Ca^{2+}]$ rise was correlated with the bouton diameter (Fig. 3*F*). The slope of this plot yielded an estimate for the Ca^{2+}-channel density of 45/μm^2, a value somewhat larger than that obtained for pyramidal-cell boutons (Koester and Sakmann, 2000). A fixed Ca^{2+}-channel density provides a perspective on the issue of whether transiently high $[Ca^{2+}]$ in a microdomain or spatially averaged $[Ca^{2+}]$ is most relevant to neurotransmitter release. A constant Ca^{2+}-channel density will produce lower spatially averaged Ca^{2+} rises for larger boutons, but Ca^{2+} transients in microdomains should be independent of diameter. Thus, different-sized boutons with the same Ca^{2+}-channel density would release transmitter with equal efficacy if the release site sees $[Ca^{2+}]$ within a microdomain.

Constancy of $\Delta[Ca^{2+}]_t$

Our analysis of endogenous Ca^{2+} buffers depends critically on the assumption of constant increments in total $[Ca^{2+}]$ ($\Delta[Ca^{2+}]_t$) during the first few action potentials of a train. If $[Ca^{2+}]_t$ decreases with successive action potentials, then Equation 10 would yield smaller values of κ_E. Figure 5*D* would then show an inverse correlation as observed but without endogenous buffer saturation. In contrast, increases in $\Delta[Ca^{2+}]_t$ would hide saturation or make it appear weaker. Thus, changes in $\Delta[Ca^{2+}]_t$ would introduce errors in our estimates of $[B]_t$ and K_b, and for sufficiently large decreases, render our interpretation of buffer saturation incorrect.

Recordings from mossy fiber boutons in the hippocampus indicate that changes in $\Delta[Ca^{2+}]_t$ are in the positive direction and too small to produce significant errors in our analysis (Geiger and Jonas, 2000). Action potentials broaden during trains and Ca^{2+}-entry increases, but these effects are quite small for the first several spikes. In 20 Hz trains, action potentials should broaden by ~0.7% per action potential [based on the stated value of 1.3% at 50 Hz and visual examination of Fig. 3 from Geiger and Jonas (2000)]. The increases in $\Delta[Ca^{2+}]_t$ were smaller than the increases in action potential width, most likely because of Ca^{2+} channel inactivation. A repeat of our own analysis, in which κ_E was calculated with a large (3%) increase in $\Delta[Ca^{2+}]_t$ per spike,

left the inverse correlation between κ_E and $[Ca^{2+}]$ strong ($p = 0.017$) and the parameter values from fitting Equation 11 essentially unchanged. In addition, the two data points in Figure 5*D* most vulnerable to changes in $\Delta[Ca^{2+}]_t$ were from the fifth and sixth action potentials of trains with 100 μM OGB1. Excluding these two points had essentially no effect ($p = 0.019$).

The assumption of constant $\Delta[Ca^{2+}]_t$ can be evaluated more directly with our data. With 100 μM OGB1, $\Delta[Ca^{2+}]$ is the same for the first two spikes (Fig. 5*C*). The high dye concentration limits $[Ca^{2+}]$ to a narrower range in which $\Delta[Ca^{2+}]$ is linear with $\Delta[Ca^{2+}]_t$. Similarly, Regehr et al. (1994) observed constant fluorescence increments during trains for the first 10 impulses. In that study, the $\Delta[Ca^{2+}]$ per action potential was very small, most likely because of buffering by a high dye concentration, which would make fluorescence linear with $\Delta[Ca^{2+}]_t$. Ca^{2+}-induced Ca^{2+} release is evoked by longer trains (Liang et al., 2002). However, these factors do not alter our interpretations, because they only become relevant after many action potentials. Thus, independent lines of reasoning support the assumption of constant $\Delta[Ca^{2+}]_t$. Variations in $\Delta[Ca^{2+}]_t$ are too small to alter our conclusions regarding the saturation of endogenous Ca^{2+} buffer or influence our estimates of K_b and $[B]_t$.

Endogenous Ca^{2+} buffer properties

Analysis with the aid of models that neglect endogenous Ca^{2+} buffer saturation showed $\kappa_E \sim 20$ (Fig. 4). Only the recent estimate of κ_E in dendritic spines is this low (Sabatini et al., 2002). Values in other nerve terminals (Stuenkel, 1994; Tank et al., 1995; Koester and Sakmann, 2000) as well as cell bodies (Neher, 1995) are often >100. The lowest value obtained previously in a nerve terminal was 40 in the calyx of Held (Helmchen et al., 1997), and it is interesting to note that both these calyces and mossy fiber boutons are relatively large. However, the present analysis suggests that calculating κ_E using a nonsaturable buffer model may lead to a value that is erroneously small. A saturable buffer can give rise to a nearly linear plot of $1/\Delta[Ca^{2+}]$ versus κ_D (Fig. 4*B*), but the value of κ_E obtained by fitting Equation 5 is much lower than κ_E computed from K_b and $[B]_t$ with Equation 4. This can be visualized by noting that as κ_D is reduced, $\Delta[Ca^{2+}]$ rises grow larger. The saturation of endogenous buffer enhances this effect, increasing the slope and shifting the *x*-intercept toward zero. Thus, the presence of a saturable buffer gives rise to a systematic error in the value of κ_E derived from a model based on nonsaturable buffer.

The analysis of $[Ca^{2+}]$ signals during trains indicated that endogenous Ca^{2+} buffers are saturated as $[Ca^{2+}]$ rises (Fig. 5*D*). The reduction of buffering strength with increasing $[Ca^{2+}]$ indicates that the endogenous Ca^{2+}-binding molecules have a K_b of $\sim$500 nM and a concentration of $\sim$130 μM. Cytoplasmic molecules that bind Ca^{2+} include both small molecules such as ATP (Baylor and Hollingworth, 1998) and proteins such as parvalbumin, calretinin, and calbindin-D28K (Baimbridge et al., 1992). The K_b for ATP is $\sim$200 μM, so ATP cannot contribute to the saturable Ca^{2+} buffering seen here. Among the Ca^{2+}-binding proteins, calbindin-D28K immunoreactivity is seen in dentate granule cells, is abundant by the age of the animals used here (3–4 weeks of age), and is distributed through the entire cell, including the mossy fibers (Baimbridge, 1992). Calbindin-D28K binds four Ca^{2+} ions (Veenstra et al., 1997) with dissociation constants ranging from 286 to 1790 nM (average, 400 nM) in 150 mM KCl and 2 mM $MgCl_2$ (Berggard et al., 2002). Our estimate of $K_b = 500$ nM is consistent with these measurements. Granule-cell axons most likely contain a spectrum of Ca^{2+}-binding molecules, but the anatomical distribution together with the binding properties make calbindin-D28K an excellent candidate for the saturable Ca^{2+} binding revealed by our experiments.

Implications for Ca^{2+}-triggered release

An analysis of Ca^{2+} diffusion in the presence of mobile buffer yielded the following expression for free $[Ca^{2+}]$ as a function of radial distance (r) from a Ca^{2+} channel for a steady state that forms in a few microseconds of channel opening (Neher, 1998), as follows:

$$[Ca^{2+}] = [Ca^{2+}]_0 + \frac{i_{Ca}}{4\pi F D_{Ca} r} e^{-r/\lambda}. \qquad (12)$$

The i_{Ca} is the single channel current (0.2 pA), F is Faraday's constant, D_{Ca} is the Ca^{2+} diffusion constant (2.2×10^{-6} cm^2/sec), and $\lambda = \lambda = \sqrt{D_{Ca}/(k_{on}[B]_f)}$, with k_{on} as the Ca^{2+}-to-buffer binding rate constant and $[B]_f$ as the free buffer concentration. With $[B]_f = 110$ μM from the present study and $k_{on} = 8 \times 10^7$ M^{-1} sec^{-1} (Nägerl et al., 2000), we obtain $\lambda = 160$ nm. With our estimate of the Ca^{2+} channel density of 45 μm^2, the mean distance between channels is $\sim$150 nm. Because this is comparable with λ, Ca^{2+}-channel microdomains would overlap and allow Ca^{2+} from different channels to summate at release sites, even without channel clustering. A release site in the center of a square of four Ca^{2+} channels would be $\sim$100 nm from each channel. Summation of $[Ca^{2+}]$ from Equation 12 for these four channels gave 15 μM. This represents an estimate for the minimum $[Ca^{2+}]$ at a release site. However, a release site that is close to a Ca^{2+} channel, say 10 nm away, would see $[Ca^{2+}] = 70$ μM; this value is insensitive to the buffer. Because single action potentials in granule cells evoke large synaptic responses (Henze et al., 2000), these estimates provide a range for $[Ca^{2+}]$ that triggers release from these boutons.

Implications for synaptic plasticity

Theoretical studies of Ca^{2+} dynamics have indicated that buffer saturation can play a role in synaptic facilitation (Neher, 1998). The introduction of exogenous buffers presynaptically results in facilitation of neocortical synapses, with synapse-specific differences that most likely reflect variations in the distance between Ca^{2+} channels and release sites (Rosov et al., 2001). For the maximum distance of 100 nm estimated above, Equation 12 suggests that buffer saturation could amplify $[Ca^{2+}]$ rises by up to twofold. This would enhance synaptic transmission during repetitive activity and provide a basis for the correlation between free $[Ca^{2+}]$ and short-term facilitation (Regehr et al., 1994).

Different laboratories have reported long-term potentiation of mossy fiber synapses that is triggered presynaptically (Ito and Sugiyama, 1991; Castillo et al., 1994; Mellor and Nicoll, 2001) and postsynaptically (Yeckel et al., 1999). The question of whether granule-cell synapses on hilar neurons also exhibit synaptic plasticity has yet to be studied. The amplification of Ca^{2+} signals by saturation of endogenous Ca^{2+} buffers would increase the effectiveness with which repetitive activity initiates Ca^{2+}-dependent signaling cascades and thus contribute to the presynaptic induction of LTP.

References

Acsady L, Kamondi A, Sik A, Freund T, Buzsaki G (1998) GABAergic cells are the major postsynaptic targets of mossy fibers in the rat hippocampus. J Neurosci 18:3386–3403.

Augustine GJ (2001) How does calcium trigger neurotransmitter release? Curr Opin Neurobiol 11:320–326.

Baimbridge KG (1992) Calcium binding proteins in the dentate gyrus. In: The dentate gyrus and its role in seizures (Ribak CE, Gall CM, Mody I, eds), pp 211–220. New York: Elsevier Science.

Baimbridge KG, Celio MR, Rogers JH (1992) Calcium-binding proteins in the nervous system. Trends Neurosci 15:303–308.

Baylor SM, Hollingworth S (1998) Model of sarcomeric Ca^{2+} movements, including ATP Ca^{2+} binding and diffusion, during activation of frog skeletal muscle. J Gen Physiol 112:297–316.

Berggard T, Miron S, Onnerfjord P, Thulin E, Akerfeldt KS, Enghild JJ, Akke M, Linse S (2002) Calbindin D_{28k} exhibits properties characteristic of a Ca^{2+} sensor. J Biol Chem 277:16662–16672.

Burrone J, Neves G, Gomis A, Cooke A, Lagnado L (2002) Endogenous calcium buffers regulate fast exocytosis in the synaptic terminal of retinal bipolar cells. Neuron 33:101–112.

Castillo PE, Weisskopf MG, Nicoll RA (1994) The role of Ca^{2+} channels in hippocampal mossy fiber synaptic transmission and long-term potentiation. Neuron 12:261–269.

Claiborne BJ, Amaral DG, Cowan WM (1986) A light and electron microscopic analysis of the mossy fibers of the rat dentate gyrus. J Comp Neurol 246:435–458.

Cox CL, Denk W, Tank DW, Svoboda K (2000) Action potentials reliably invade axonal arbors of rat neocortical neurons. Proc Natl Acad Sci USA 97:9724–9728.

DiGregorio DA, Vergara JL (1997) Localized detection of action potential-induced presynaptic calcium transients at a *Xenopus* neuromuscular junction. J Physiol (Lond) 505:585–592.

Emptage NJ, Reid CA, Fine A (2001) Calcium stores in hippocampal synaptic boutons mediate short-term plasticity, store-operated Ca^{2+} entry, and spontaneous transmitter release. Neuron 29:197–208.

Geiger JRP, Jonas P (2000) Dynamic control of presynaptic Ca^{2+} inflow by fast-inactivating K^+ channels in hippocampal mossy fiber boutons. Neuron 28:927–939.

Helmchen F, Borst GG, Sakmann B (1997) Calcium dynamics associated with a single action potential in a CNS presynaptic terminal. Biophys J 72:1458–1471.

Henze DA, Urban NN, Barrionuevo G (2000) The multifarious hippocampal mossy fiber pathway: a review. Neuroscience 98:407–427.

Holthoff K, Tsay D, Yuste R (2002) Calcium dynamics of spines depend on their dendritic location. Neuron 33:425–437.

Ito I, Sugiyama H (1991) Roles of glutamate receptors in long-term potentiation at hippocampal mossy fiber synapses. NeuroReport 2:333–336.

Jackson MB, Konnerth A, Augustine GJ (1991) Action potential broadening and frequency-dependent facilitation of calcium signals in pituitary nerve terminals. Proc Natl Acad Sci USA 88:380–384.

Koester HJ, Sakmann B (2000) Calcium dynamics associated with action potentials in single nerve terminals of pyramidal cells in layer 2/3 of the young rat neocortex. J Physiol (Lond) 529:625–646.

Liang Y, Yuan L-L, Johnston D, Gray R (2002) Calcium signaling at mossy fiber presynaptic terminals in the rat hippocampus. J Neurophysiol 87:1132–1137.

Maravall M, Mainen ZF, Sabatini BL, Svoboda K (2000) Estimating intracellular calcium concentrations and buffering without wavelength ratioing. Biophys J 78:2655–2667.

Meinrenken CJ, Borst JGG, Sakmann B (2002) Calcium secretion coupling at calyx of Held governed by nonuniform channel-vesicle topography. J Neurosci 22:1648–1667.

Melamed N, Helm PJ, Rahamimoff R (1993) Confocal microscopy reveals coordinated calcium fluctuations and oscillations in synaptic boutons. J Neurosci 13:632–649.

Mellor J, Nicoll RA (2001) Hippocampal mossy fiber LTP is independent of postsynaptic calcium. Nat Neurosci 4:125–126.

Nägerl UV, Novo D, Mody I, Vergara JL (2000) Binding kinetics of calbindin-D_{28k} determined by flash photolysis of caged Ca^{2+}. Biophys J 79:3009–3018.

Neher E (1995) The use of fura-2 for estimating Ca buffers and Ca fluxes. Neuropharmacology 34:1423–1442.

Neher E (1998) Usefulness and limitations of linear approximations to the understanding of Ca^{2+} signals. Cell Calcium 24:345–357.

Neher E, Augustine GJ (1992) Calcium gradients and buffers in bovine chromaffin cells. J Physiol (Lond) 450:273–301.

Regehr WG, Tank DW (1991a) Selective fura-2 loading of presynaptic terminals and nerve cell processes by local perfusion in mammalian brain slices. J Neurosci Methods 37:111–119.

Regehr WG, Tank DW (1991b) The maintenance of LTP at hippocampal mossy fiber synapses is independent of sustained presynaptic calcium. Neuron 7:451–459.

Regehr WG, Delaney KR, Tank DW (1994) The role of presynaptic calcium in short-term enhancement at the hippocampal mossy fiber synapse. J Neurosci 14:523–537.

Roberts WM (1994) Localization of calcium signals by a mobile calcium buffer in frog saccular hair cells. J Neurosci 14:3246–3262.

Rosov A, Burnashev N, Sakmann B, Neher E (2001) Transmitter release modulation by intracellular Ca^{2+} buffers in facilitating and depressing nerve terminals of pyramidal cells in layer 2/3 of the rat neocortex indicates a target cell-specific difference in presynaptic calcium dynamics. J Physiol (Lond) 531:807–826.

Sabatini BL, Oertner TG, Svoboda K (2002) The life cycle of Ca(2+) ions in dendritic spines. Neuron 33:439–452.

Scharfman HE (1993) Characteristics of spontaneous and evoked EPSPs recorded from dentate spiny hilar cells in rat hippocampal slices. J Neurophysiol 70:742–757.

Scharfman HE, Kunkel DD, Schwartzkroin PA (1990) Synaptic connections of dentate granule cells and hilar neurons: results of paired intracellular recordings and intracellular horseradish peroxidase injections. Neuroscience 37:693–707.

Smith SJ, Osses LR, Augustine GJ (1988) Fura-2 imaging of localized calcium accumulation within squid "giant" presynaptic terminal. In: Calcium and ion channel modulation (Grinnell AD, Armstrong D, Jackson MB, eds), pp 147–155. New York: Plenum.

Stuenkel EL (1994) Regulation of intracellular calcium and calcium buffering properties of rat isolated neurohypophysial nerve endings. J Physiol (Lond) 481:251–271.

Tank DW, Regehr WG, Delaney KR (1995) A quantitative analysis of presynaptic calcium dynamics that contribute to short-term enhancement. J Neurosci 15:7940–7952.

Umbach JA, Saitoe M, Kidokoro Y, Gundersen CB (1998) Attenuated influx of calcium ions at nerve endings of *csp* and *shibire* mutant *Drosophila*. J Neurosci 18:3233–3240.

Veenstra TD, Johnson KL, Tomlinson AJ, Naylor S, Kumar R (1997) Determination of calcium binding sites in rat brain calbindin D28K by electrospray ionization mass spectrometry. Biochemistry 36:3535–3542.

Yamada WM, Zucker RS (1992) Time course of transmitter release calculated from simulations of a calcium diffusion model. Biophys J 61:671–682.

Yeckel MF, Kapur A, Johnston D (1999) Multiple forms of LTP in hippocampal CA3 neurons use a common postsynaptic mechanism. Nat Neurosci 2:625–633.